

Surface deformation and landslides caused by the 6th nuclear test of North Korea on September 3, 2017 detected by satellite SAR and InSAR techniques

Jisang Yoon¹, Hoonyol Lee^{1*}, Jung-Ho Park², Chang Soo Cho², Geunyoung Kim², and Hyun-Moo Cho²

¹Department of Geophysics, Kangwon National University, Chuncheon 24341, Republic of Korea

²Earthquake Research Center, Geology Division, Korea Institute of Geosciences and Mineral Resources, Daejeon 34132, Republic of Korea

ABSTRACT: The 6th nuclear test of North Korea on September 3, 2017 produced an m_b 6.1 artificial earthquake and significant surface deformations detectable from satellite observations. Wang et al. (2018) have reported the surface displacement of the Mt. Mantap caused by the explosion by applying offset-tracking method to TerraSAR-X SAR images. Based on the assumption of elastic behaviour of the mountain body, they have modelled the rise and collapse of the mountain and suggested the location, depth and energy of the explosion. However, we suspect that the surface displacement might be caused by landslide in which case the elastic modelling would be misleading. In this paper, we use both SAR interferometry and offset-tracking method to quantify the elastic and random deformation caused by the explosion. The 3-D displacement vectors around the rim of the explosion, where the interferometric coherence is maintained, were obtained by using three ALOS-2 interferograms acquired in different orbits. Only east-west component of the displacement vector was valid due to orbital characteristics, which indicates the explosive tendency of the bedrock of up to 25 cm in the rim of the mountain. Deformation on the ruptured zone, where the interferometric coherence is lost, was detected through visual inspection and offset tracking by using two pairs of high-resolution ALOS-2 and TerraSAR-X images. It showed up to 3.5 m displacement on the mountain slope towards the direction of gravity, which is similar to the results of Wang et al. (2018). However, we have visually identified many stable points and features that have not moved at all in the mountain flank surrounded by active surface deformation, which is believed to be stable bedrocks and outcrops. This implies that the displacements observed by the offset method in the mountain flank of the ruptured zone were mostly of landslides caused by the topsoil and boulder stones. It is suggested that elastic behaviour of the mountain body due to the 6th nuclear test of North Korea is unidentifiable and the subsequent modelling might be invalid in the mountain flank of the ruptured zone where surface motion from landslides is dominant.

Key words: nuclear test, surface displacements, InSAR, visual inspection, offset tracking

Manuscript received February 9, 2020; Manuscript accepted September 3, 2020

1. INTRODUCTION

Nuclear tests produce strong artificial earthquakes and large surface displacements. Although the scale can be estimated through the size of the crater and the deformation, most of the cases are carried out secretly under the basement. Therefore, the access to the site is limited and the research through the direct approach is insufficient. (Teller et al., 1968; Glasstone and Dolan, 1977). In this regard, studies using high-resolution satellite images have been used for areas with virtually limited access. In particular, Synthetic Aperture Radar (SAR) is effective to detect changes on the land surface with less influence of daylight and weather conditions due to the use of microwaves (Curlander

*Corresponding author:

Hoonyol Lee
Department of Geophysics, Kangwon National University, Chuncheon 24341, Republic of Korea
Tel: +82-33-250-8587, Fax: +82-33-259-5669,
E-mail: hoonyol@kangwon.ac.kr

Electronic supplementary material

The online version of this article (<https://doi.org/10.1007/s12303-020-0057-0>) contains supplementary material, which is available to authorized users.

©The Association of Korean Geoscience Societies and Springer 2021

and McDonough, 1991). Interferometric SAR (InSAR) technique that uses the differences in the phase of the microwave between SAR images was also used to observe the deformation by the nuclear tests in Nevada, United States or in China (Vincent et al., 2003, 2011).

Since 2006, North Korea has conducted nuclear tests for 6 times in the test site of Mt. Mantap located in Punggye-ri, Gilju-gun, Hamgyongbuk-do. These have been observed and studied by using various methods such as infrasound, seismic waves, satellite images, and modelling techniques to estimate the location and depth of the epicentre and hypocentre, the surficial movement, and the scale of explosions (Zhang and Wen, 2013; Che et al., 2014; Wei, 2017; Lee et al., 2018; Stevens and O'Brien, 2018; Tian et al., 2018; Wang et al., 2018). The tendency in explosive yield of those tests has generally been increasing. In particular, the 6th nuclear test conducted on September 3, 2017 was the largest test that had involved a significant amount of surface deformation (Pavian and Coblenz, 2017). In this regard, it was estimated to be m_b (body-wave magnitude scale) 6.1 equivalent to 126–146 kilo ton by Korea Institute of Geoscience and Mineral Resources (Park et al., 2017) and Norwegian Seismic Array (NORSAR, 2017), and to be m_b 6.3 by United States Geological Survey (USGS, 2017). It was about nine times larger in terms of the released energy than the previous 5th nuclear test conducted on September 9, 2016 (Stevens and O'Brien, 2018).

As previous studies, Wang et al. (2018) analysed the 3-D surface displacement caused by the 6th nuclear test by applying offset tracking technique to TerraSAR-X images. In addition, the source model was performed in comparison with the surface displacement to estimate the location, depth, and the scale of the detonation. Moreover, the model was constructed by assuming that the bedrock of Mt. Mantap is a uniform elastic medium and followed the scenario of an elastic explosion (expansion), collapse, and compaction. The authors have noted that there may be some problems in the model if the bedrock has a non-uniform structure and there are surficial processes such as landslides (Wang et al., 2018).

Lee et al. (2018) analysed the coherence map to distinguish the damaged surface area, and presented the statistical result of the offset tracking method using ALOS-2 images. Even though they suspected landslides and collapse area through the optical images of Pleiadas-A/B, visual inspection observations of SAR images were not performed in detail. The resolution of offset tracking is several tens of pixels depending on the window size used for cross-correlation, but in the case of visual inspection with human eyes, it has the resolution of a pixel. In addition, the offset tracking method uses only cross-correlation of the amplitude values that might be biased by prominent features not relevant to offset but change of backscattering coefficient, but human

eyes produce better results of feature tracking and comparison between images.

Based on our preliminary results on visual inspection of the geo-coded SAR images, however, we found that there are many stable targets on the slopes of Mt. Mantap where surface deformation occurred downslope (Yoon and Lee, 2019). We suspect that the offset tracking results are of landslide rather than elastic motion of the mountain body, which might invalidate the elastic assumption and the modelling results of Wang et al. (2018). Wei (2017) also proposed two possibilities in the interpretation of the InSAR signal obtained from the 4th nuclear test at the same site occurred on 6 January 2016: one is the triggered landslide and the other is the uplift of the mountain. Only the latter case allows the estimation of the location, depth and cavity size using elastic modelling. The possibility of the landslide cannot be neglected for the 6th nuclear test because the magnitude (m_b 6.1–6.3) exceeds the minimum threshold of around M_L 4.5 for soil block slides and M_L 5.0 for rock block slides caused by earthquakes (Keeper, 1984).

In this study, the detection of surface deformation of the 6th nuclear test was conducted by analysing SAR images similar to Wang et al. (2018), but from a different perspective. SAR data of ALOS-2 and TerraSAR-X were used in the study area, but different SAR techniques were applied to depending on the type of the surface deformation. InSAR technique was used to obtain three-dimensional surface displacements around the rim of the Mt. Mantap where the coherence is maintained sufficiently for ALOS-2 interferograms from three different orbits. Using high-resolution TerraSAR-X images, visual inspection and offset tracking technique were performed to detect characteristics of the surface deformation on the ruptured zone where the interferometric coherence is low.

Chapter 2 describes the study area and data used in this study followed by the methods such as InSAR, visual inspection, and offset tracking in Chapter 3. Chapter 4 reports the results from each method and discussion followed by the conclusion in Chapter 5.

2. STUDY AREA AND DATA

2.1. Study Area

The nuclear test site is located in Punggye-ri, Gilju-gun, Hamgyongbuk-do, North Korea, where several tunnels were built inside Mt. Mantap (Fig. 1). The altitude of the mountain is 2205 m and the bedrock consists of hard granite overlain by about 200 m of volcanic sediments such as trachyte and basalt (Pavian and Coblenz, 2017). Although the hard and stable bedrock was considered as a suitable area for nuclear tests due to a low risk of radioactive spillage, it has a high potential of surficial landslides due to the presence of volcanic sediments.

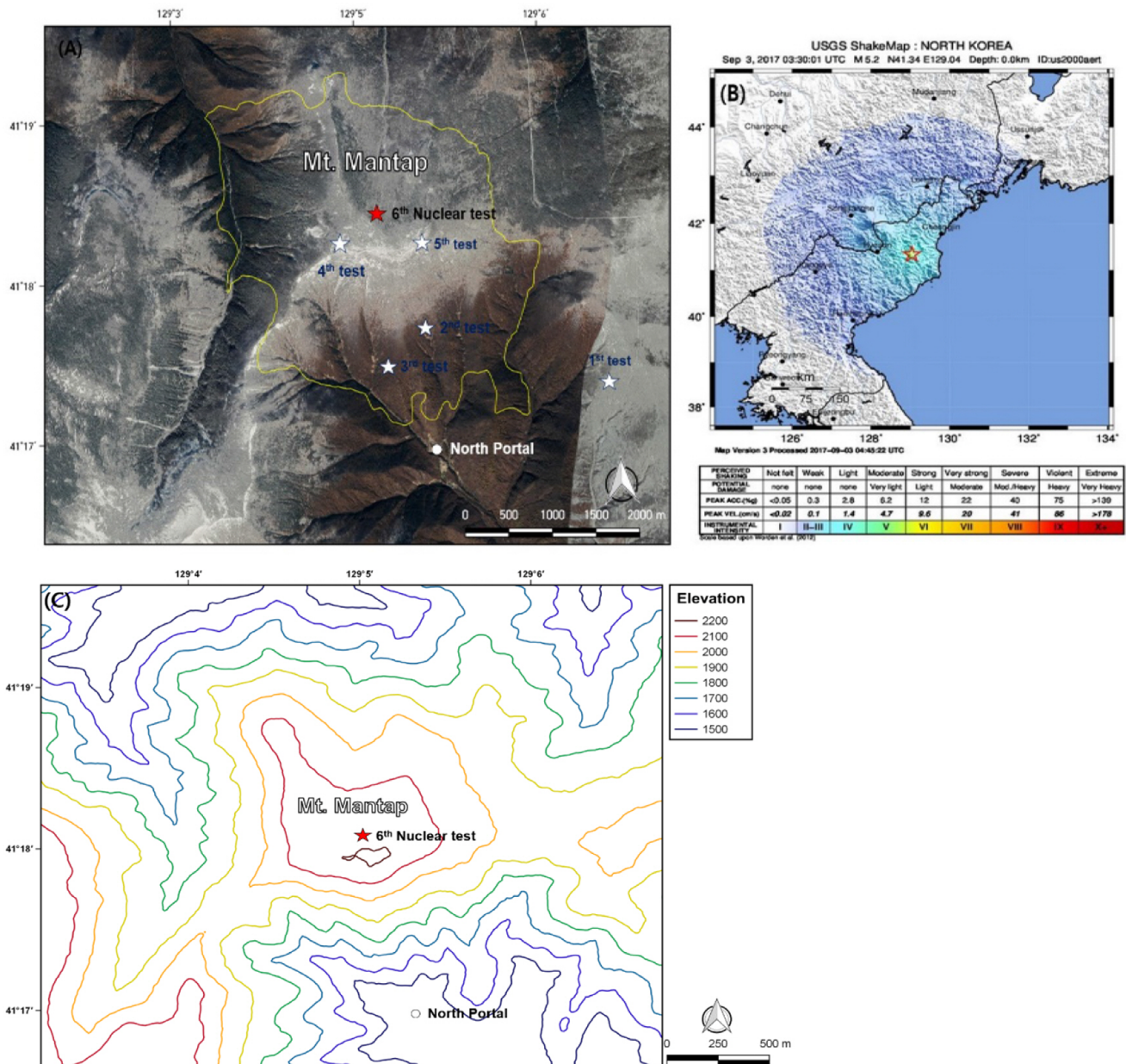


Fig. 1. The study area and the shake map of the 6th nuclear test on September 3, 2017. (a) Google Earth image representing the study area over Mt. Mantap. The red star and white stars indicate the 6th nuclear test on 3 September 2017 and the previous tests, respectively. The inner part of the yellow line indicates the ruptured zone with low interferometric coherence. The location of the north portal is presented as a white dot. (b) The shake map that shows the location and the intensity of the earthquake from the test (USGS, 2017). (c) Elevation contours of the study area.

2.2. Data

SAR images acquired by ALOS-2 operating in Japanese Aerospace Exploration Agency (JAXA) and TerraSAR-X operating in German Aerospace Centre (DLR) were used in this study (Table 1). ALOS-2 PALSAR-2, launched in May, 2014, is equipped with L-band (a centre frequency of 1.2 GHz and a wavelength of 24 cm) and revisits the same ground track every 14 days (JAXA, 2014). The used images are Single Look Complex (SLC, level 1.1), acquired

in strip-map mode with right-looking, in HH-polarization. Three interferograms were obtained by using six images that were acquired in three different tracks (two in ascending orbits and one in descending orbit) to get three-dimensional surface displacements of the rim part. Among them, four UBS (Ultra-fine mode Single polarization) images with the resolution better than 3 m were also used for visual inspection and offset tracking to detect the general tendency of deformation on the ruptured zone. Although the general trend of offset tracking has already been obtained by

Table 1. List of SAR data used in this study

Name	Pair 1 (FBD ^(a))	Pair 2 (UBS ^(b))	Pair 3 (UBS)	Pair 4	Pair 5
Platform	ALOS-2 PALSAR-2			TerraSAR-X	
Track	Ascending	Ascending	Descending	Ascending	Descending
Acquisition Date (yyyy/mm/dd)	2017/07/27	2017/08/29	2017/08/31	2017/06/05	2017/08/24
	2017/09/07	2017/09/12	2017/09/28	2017/09/12	2017/09/04
Perpendicular baseline (m)	41.11	-11.8	-61.95	-374.16	-156.21
Temporal baseline (days)	42	14	28	99	11
Incidence Angle (°)	34.08	43.47	37.53	33.6	48.3
Range pixel spacing (m)	4.29	1.43	1.43	0.45	0.45
Azimuth pixel spacing (m)	3.96	1.94	2.23	0.86	0.86

^(a)FBD: Fine mode Dual polarization.

^(b)UBS: Ultra-fine mode Single polarization.

using these image pairs in the previous research of Lee et al. (2018), it is required to visually observe the characteristics of features in the SAR images.

TerraSAR-X was launched on 15 June 2007 that acquires SAR images in the same ground track in every 11 days. High-resolution images of up to 1 m are used in this study by using the X-band antenna with a centre frequency of 9.6 GHz in spotlight mode, HH-polarization, right-looking as level 1B SSC (Single Look Slant Range Complex) format. Visual inspection and offset tracking were adopted by using four images acquired before and after the event in two different tracks (one in ascending and the other in descending orbit) for the detection of deformation at the ruptured zone.

3. METHODS

SNAP (Sentinel Application Platform) software developed by ESA (European Space Agency) was mainly used for InSAR processing and offset tracking method in this study. Algorithms of the data processing were designed and performed by using the graph builder of SNAP, and final images were visualized in Google Earth for visual inspection.

3.1. InSAR Displacements Extraction

We used Differential InSAR (DInSAR) method to detect surficial changes of the rim part of the mountain that maintains coherence for ALOS-2 PALSAR-2 data following the steps shown in Figure 2 (Lee, 2006; Ferretti et al., 2007; Zhou et al., 2009).

Firstly, two SAR images acquired before (the slave image) and after (the master image) the event were stacked and co-registered with each other to generate initial interferogram. The flat-earth phase and topographic phase were removed by using the orbit data and SRTM (Shuttle Radar Topography Mission) 1 arc second DEM, after which signal to noise ratio was improved by applying

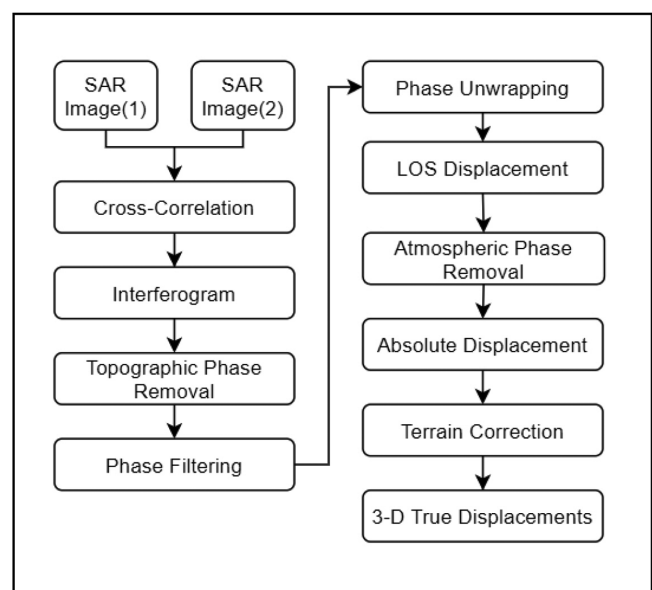


Fig. 2. Flowchart of DInSAR and subsequent processes.

Goldstein Phase Filter (Fialko et al., 2005; Jarvis et al., 2008; Veci, 2016; Song and Lee, 2018). Phase unwrapping was performed by the snaphu software (Chen and Zebker, 2002), and the LOS (Line of Sight) displacements were obtained (Bamler and Hartl, 1998; Zhou et al., 2009; Yoon et al., 2010). The atmospheric effect was reduced statistically assuming that the horizontally homogeneous atmospheric hydrostatic delay is a function of the topographic elevation (Berardino et al., 2002). To overcome uncertainty in the absolute displacement, zero displacement was determined statistically over a stable region after which a low coherence (< 0.3) was masked out.

A minimum of three interferograms formed by SAR images acquired in different look directions is required in order to extract information of actual displacement vector in 3-D (Ng et al., 2011). The LOS displacement vector $R = [r_1 \ r_2 \ r_3]^T$ obtained from the three DInSAR images can be expressed as a matrix

multiplication of a LOS unit matrix L and a true displacement vector $\mathbf{D} = [x \ y \ z]^T$ has easting, northing, and vertical components as follows (Fialko et al., 2001; Wright et al., 2004).

$$\mathbf{R} = \mathbf{L}\mathbf{D}, \tag{1}$$

$$\text{where } \mathbf{L} = \begin{bmatrix} -\sin \theta_1 \cos \alpha_1 & \sin \theta_1 \cos \alpha_1 & \cos \theta_1 \\ -\sin \theta_2 \cos \alpha_2 & \sin \theta_2 \cos \alpha_2 & \cos \theta_2 \\ -\sin \theta_3 \cos \alpha_3 & \sin \theta_3 \cos \alpha_3 & \cos \theta_3 \end{bmatrix},$$

so that a true displacement can be found by $\mathbf{D} = \mathbf{L}^{-1}\mathbf{R}$. Here, θ_i ($i = 1, 2, 3$) are the local incidence angles for three DInSAR images, and α_i ($i = 1, 2, 3$) are the satellite headings projected on the horizontal plane measured clockwise from North, respectively. For our dataset, L is composed of three interferograms, generated with the ascending pair acquired on 27 July 2017 and 7 September 2017, the ascending pair acquired on 29 August 2017 and 12 September 2017, and the descending pair acquired on 31 August 2017 and 28 September 2017. In this case, Equation (1) has the following components.

$$\begin{bmatrix} r_1 \\ r_2 \\ r_3 \end{bmatrix} = \begin{bmatrix} 0.5526 & 0.0987 & -0.8284 \\ 0.6806 & 0.1117 & -0.7258 \\ -0.5996 & 0.1074 & -0.7930 \end{bmatrix} \begin{bmatrix} x \\ y \\ z \end{bmatrix}. \tag{2}$$

The true displacement vector (D) is then,

$$\begin{bmatrix} x \\ y \\ z \end{bmatrix} = \begin{bmatrix} 0.4138 & 0.4166 & -0.8135 \\ -37.9564 & 36.3997 & 6.3357 \\ -5.4535 & 4.6148 & 0.2122 \end{bmatrix} \begin{bmatrix} r_1 \\ r_2 \\ r_3 \end{bmatrix}. \tag{3}$$

Derivation of (3) defines the uncertainties of the measurement that results in,

$$\begin{bmatrix} \delta x \\ \delta y \\ \delta z \end{bmatrix} = \begin{bmatrix} 0.4138 & 0.4166 & -0.8135 \\ -37.9564 & 36.3997 & 6.3357 \\ -5.4535 & 4.6148 & 0.2122 \end{bmatrix} \begin{bmatrix} \delta r_1 \\ \delta r_2 \\ \delta r_3 \end{bmatrix}, \tag{4}$$

where δr_1 , δr_2 , and δr_3 are the LOS displacement error. The maximum displacement errors in each components, ($\varepsilon_x, \varepsilon_y, \varepsilon_z$), can be defined as the maximum value of the inner product of each row vector of 3×3 matrix and the LOS displacement error vector in Equation (4). This occurs when two vectors are aligned with each other so that the maximum values are the multiplication of the norm of the two vectors. If we nominally take $\frac{\lambda}{4}$ (6 cm) of the L-band wavelength (24 cm) for the LOS displacement error, mostly due to the atmospheric effect and uncertainties of phase measurement, they are roughly ($\varepsilon_x, \varepsilon_y, \varepsilon_z$) = (6 cm, 260 cm, 30 cm) for easting, northing, and vertical components, respectively. Note the uncertainty in northing direction is extremely larger than others due to the low sensitivity along the azimuth (flight) direction of SAR imagery (Ng et al.,

2011). Therefore, displacement components lower than those errors should be excluded from interpretation.

3.2. Visual Inspection

The interferometric coherence is totally lost on the ruptured zone where drastic deformation occurred in a short term, which is called temporal decorrelation (Lee et al., 2018; Wang et al., 2018). The central area of the nuclear explosion has undergone severe surface motion in a random fashion that coherence is lost for X-band and L-band SAR interferogram. Therefore, SAR amplitude images are radiometrically and geometrically corrected for visual inspection to recognize surficial changes.

SAR images acquired in slant range were converted into ground range detected images as a pre-processing, after which co-registration was performed by using accurate orbit data and SRTM 1 arc second DEM to collocate two images based onto a reference (master) geometry. The region of the study was then extracted by spatial subset, and was exported to the Google Earth KMZ format using the Range Doppler Terrain Correction function in SNAP software. A tendency of surface deformation was determined by comparing image pairs acquired before and after the explosive event. The visual inspection results were also regarded as a reference to adjust the parameters for the offset tracking method. A flowchart of the processing is shown on the left side of Figure 3.

3.3. Offset Tracking

Offset tracking is often used to detect surface displacement when InSAR loses coherence due to large deformation in a

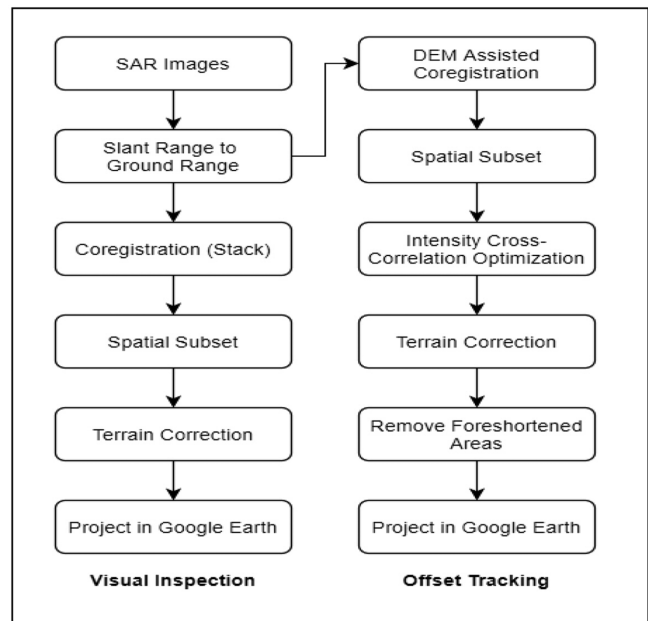


Fig. 3. Flowchart of visual inspection and offset tracking.

short time period such as landslides and glacier movement (Yan et al., 2013; Shi et al., 2015; Chae et al., 2017; Sánchez-Gómez and Navarro, 2017). Offset tracking technique uses the cross-correlation between intensities of master and slave images to obtain surface displacements and velocities. As it also gives deformation both in range and azimuth direction, offset tracking is a reasonable method to detect deformation of the central part of Mt. Mantap where coherence is lost completely.

Firstly, DEM-assisted co-registration of single look complex (SLC) images was conducted in SNAP software using a precise orbit data and SRTM 1 arc second DEM to provide a better prediction of the offset vectors around Mt. Mantap (Nitti et al., 2011; Yan et al., 2013; Lu and Veci, 2016). The window size to compute the correlation must be adjusted carefully because the accuracy and resolution of the offset tracking depend on it. High resolution is achieved when the window size is small, degrading accuracy due to low SNR for cross-correlation and local mismatch due to speckle noise. Taking a large window can improve the accuracy at a cost of low resolution. A multi-kernel method and advanced offset tracking have been designed by using statistical ways to overcome problems in offset tracking (Chae et al., 2017; Lee et al., 2018). A similar approach has been applied in this study to change the parameters such as the window size, the maximum search area, and the threshold sequentially. The final results were chosen that reasonably match the visual inspection observations. A flowchart of the offset tracking processing is shown on the right side of Figure 3.

4. RESULTS AND DISCUSSION

4.1. InSAR Displacement

3-D true displacement vectors were obtained by the three pairs of ALOS-2 PALSAR-2 DInSAR data from three different orbits. Figure 4 shows the true displacement vectors which

indicate elastic motion of the bedrock around the rim part of the mountain in easting, vertical, and northing direction respectively. In Figure 4a, displacements of 5 to 25 cm eastward on the east slope, 6 to 9 cm eastward on the south slope around the north portal, and 9 to 25 cm westward on the southwest and the northwest slopes were observed. The pattern of displacements represents a radial explosion, which is symmetrically outward with respect to the red dotted line. It is interpreted that the explosive displacement is the major pattern of the motion while any compressive displacement would be hidden in signals of expansion if any. Given the maximum error of about 6 cm in easting direction (ε_x) from Equation (4), it is considered that the signal of the true displacement vector in easting direction is valid. However, true displacement components in vertical (Fig. 4b) and northing direction (Fig. 4c) were within the error ranges ($\varepsilon_z = 30$ cm, $\varepsilon_y = 260$ cm) due to the low sensitivity in azimuth direction and vertical direction.

4.2. Visual Inspection of Displacement

Two pairs of ALOS-2 and TerraSAR-X SAR images were used for visual inspection to identify relative motion occurred before and after the event in pixel resolution. A general pattern towards the direction of gravity was observed from the ALOS-2 PALSAR-2 images provided as a motion-GIF file of Figure S1 (electronic supplementary material) flipping before and after the event. Movements were rarely observed on the top of Mt. Mantap, and a flow pattern was seen on the south-southwest and the east-southeast slopes respectively. However, signals from ALOS-2 PALSAR-2 with L-band were not distinct enough for visual inspection due to relatively low resolution and SNR.

TerraSAR-X images that have high spatial resolution of nominally less than 1 m give more detailed observation (Figs. 5, 6, and S2–S6). Figure 5 (also in Figs. S2 and S3) from images acquired on 24 August 2017 and 4 September 2017 in the descending track

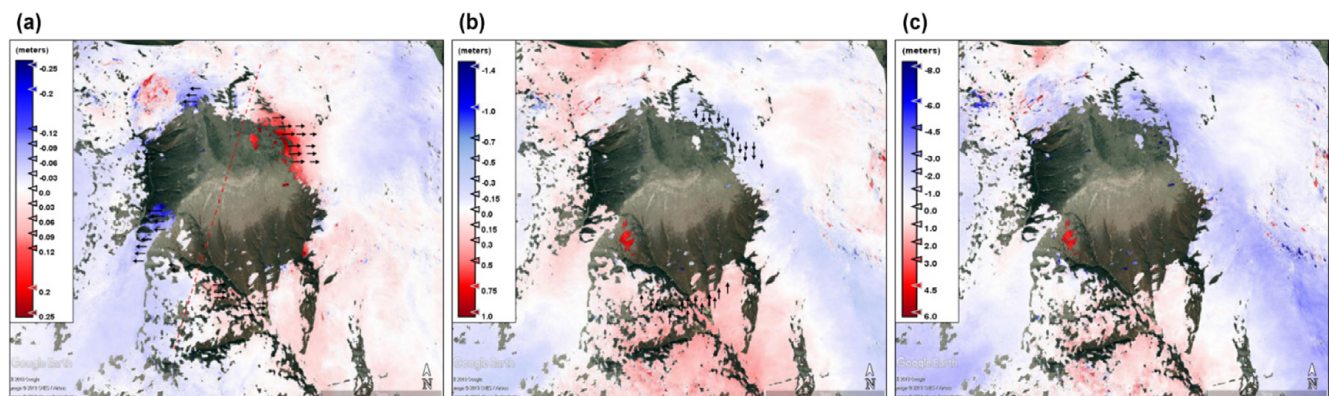


Fig. 4. The 3-D true displacement components obtained by the InSAR process. (a) In easting direction, (b) in vertical, and (c) in northing direction, respectively.

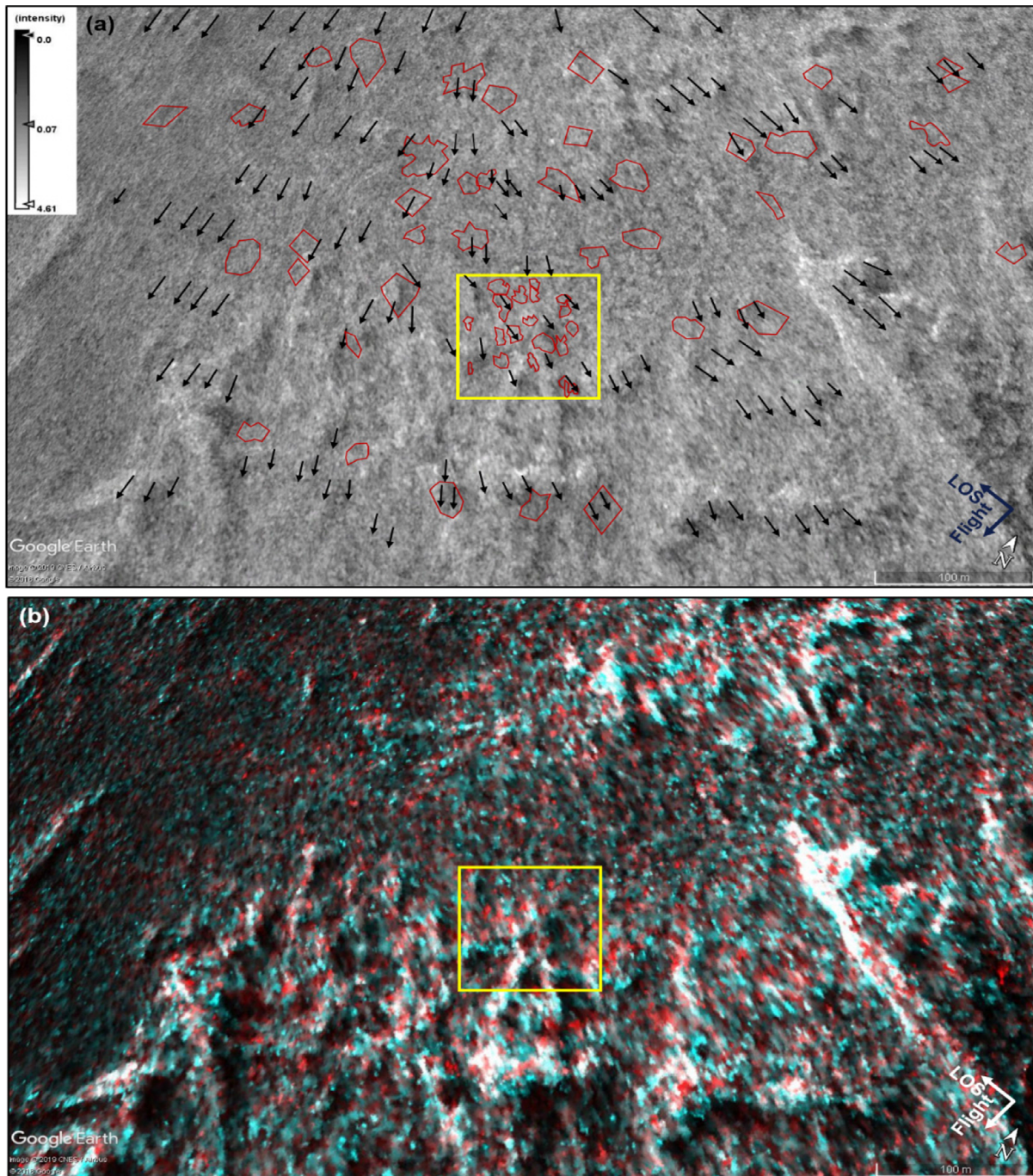


Fig. 5. The enlarged pair of the terrain corrected TerraSAR-X images of the south-southeast slope of Mt. Mantap. (a) Image acquired on 24 August 2017. The visual inspection result where stable features are marked in red polygons and moving points are shown in arrows. (b) RGB image using the master (24 August 2017) as red and the slave (4 September 2017) as green and blue layers.

shows the enlarged view on the south-southeast slope. Figure 5a shows an intensity image in the ground range acquired on 24 August 2017, and Figure 5b represents an RGB image obtained by setting the master image (24 August 2017) as red and the slave image (4 September 2017) as green and blue. First, the visual inspection observation was performed by flipping master and slave images repeatedly to recognize the motion of deformation

as shown in Figures 5a, S2, and S3. The major tendency of ground deformation is observed towards the direction of gravity. However, there are large numbers of stable features in the middle of the general pattern marked as points, lines, and polygons in Figures 5a, S2, and S3. Similar features are also visible in Google Earth's Keyhole Markup language in Zip (KMZ) format provided as supplementary data (available at <http://sar.kangwon.ac.kr/ftp/>

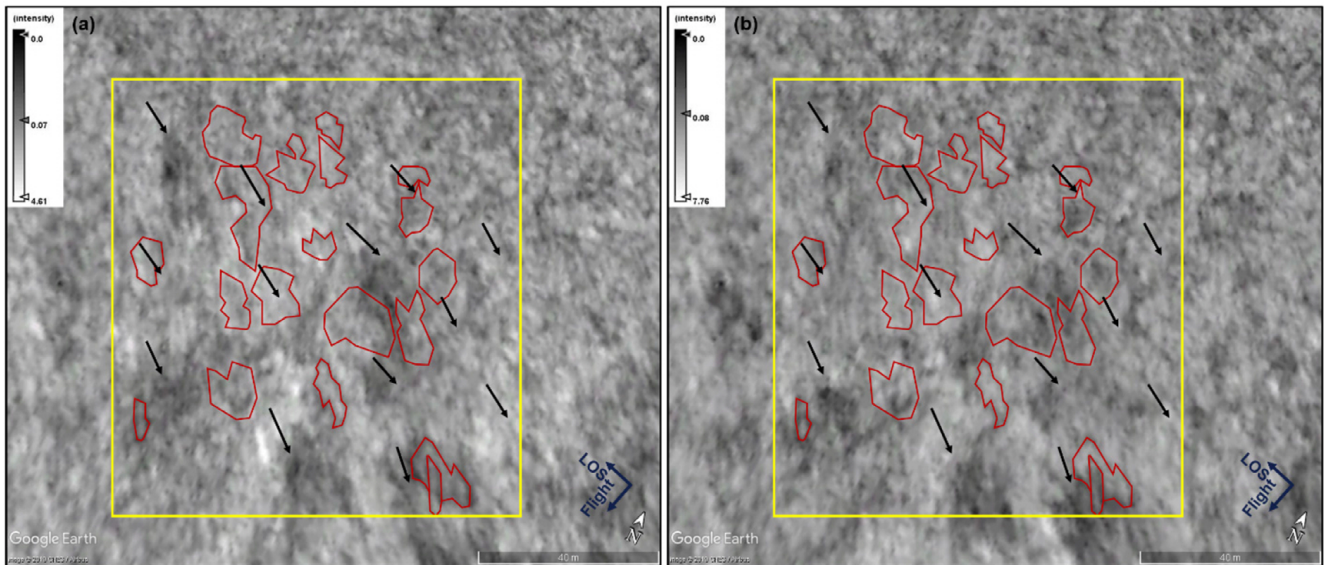


Fig. 6. Enlarged images of the area marked as a yellow box in Figure 5. The ground range detected images acquired (a) before and (b) after the event show the result of visual inspection in detail. Same polygons and arrows are overlapped onto two images, the start point of arrows in (a) and the endpoint in (b) indicate deformation during the event.

TerraSAR-X_Descending.kmz).

Subsequently, we observe the RGB image (Fig. 5b) to verify either the areas recognized through the visual comparison have been stable or moved during the event. The white to grey colour represents the stable points, whereas the red and cyan colours represent the moving points. Although it is not a completely clear pattern of the motion, the displacements are distributed in a band shape along the slope, and there are many stable points between them. As a result of the process comparing between intensity images and the RGB image above, the stable features that have not moved at all are marked in red polygons, and the moved points are shown by arrows in Figure 5a. Arrows that seem slightly exaggerated represent displacements of 4 to 6 m, and locally up to 8 m. This is because eyes can match the moving pixels that are considered as outliers by the computer algorithm.

Figure 6 (also in Figs. S4 and S5) shows enlarged features of the area marked in a yellow box in Figure 5 (Circle 1 and 2 in Figs. S4 and S5, respectively) which have remarkably stable characteristics. Surrounded by the moving pixels, those features are fixed and show no motion at all during the event. Moreover, polygonal boundaries at Figures 6a and b (also Circle 1 and 2) had not moved at all while central and surrounding pixels moved into the direction of gravity shown by arrows as the visual inspection results.

These stable points are considered as outcrops and bedrock of Mt. Mantap which does not experience any motion in terms of pixel accuracy during the event. Figure S6 from images acquired on 5 June 2017 and 12 September 2017 in the ascending track also shows many stable features on the south-southeast slope.

4.3. Offset Tracking Displacement

Offset tracking was performed by changing the parameters such as window size, threshold, and maximum velocity, and choosing the results that best represent the tendency of visual inspection as shown in Figure 7. Foreshortened areas with the projected local incidence angle less than 20 degrees were removed from the offset tracking results after the terrain correction.

The overall tendency of the displacement is distributed in the direction of gravity along the geometry of the mountain slope as shown in arrows and coloured map in Figure 7. In the ascending track of ALOS-2 PALSAR-2 (Figs. 7a and b), displacements of 2 to 2.5 m and partially up to 3 m on the east-southeast slope and of 1.8 to 2.2 m on the north slope were observed. In descending tracks of ALOS-2 PALSAR-2 (Figs. 7c and d) and TerraSAR-X (Figs. 7e and f), displacements of up to 3.5 m on the west-southwest slope, of up to 2.5 m and partially 3 m on the east-southeast slope, and of up to 2.5 m and partially 2.8 m on the north slope were observed. It is also shown that TerraSAR-X displacement map gives better resolution than ALOS-2 PALSAR-2 due to its higher resolution.

The nominal accuracy of the displacements is considered as one-fourth of the image resolution, which is approximately 0.4 m in range and 0.6 m in azimuth for ALOS-2 PALSAR-2 UBS images and 0.2 m in range and 0.3 m in azimuth for TerraSAR-X images. As the resolution is also a function of aspect and angle of each slope, however, the actual accuracy of offset tracking method is different in locations.

Overall, displacements of up to 2.5 m on the east-southeast, of

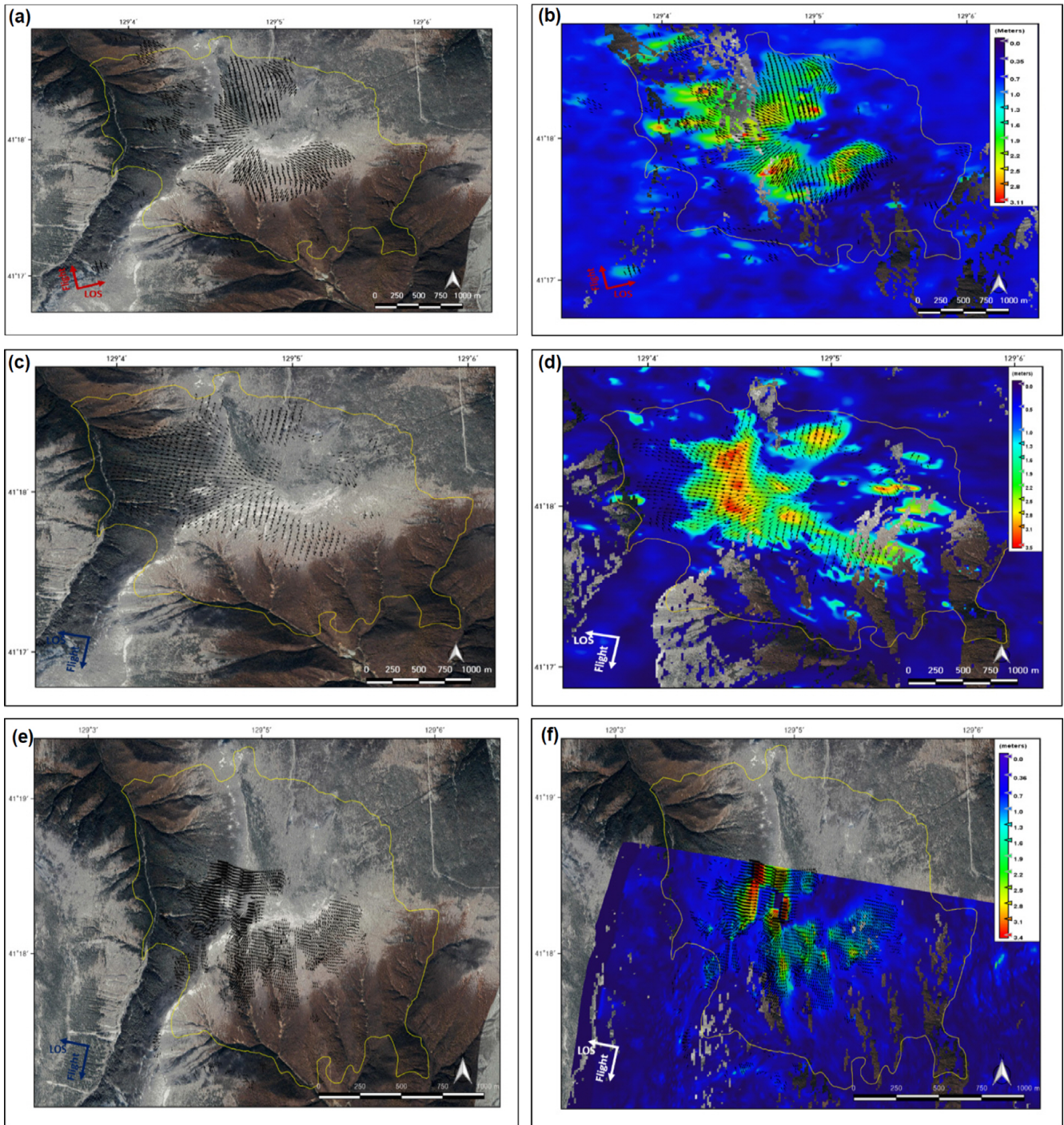


Fig. 7. Offset tracking displacements: Left-hand images show arrows over Google Earth image while right-hand images are over the displacement magnitude map. (a and b) ALOS-2 PALSAR-2 UBS images on 29 August 2017 and 12 September 2017 in the ascending track, (c and d) on 31 August 2017 and 28 September 2017 in the descending track, and (e and f) TerraSAR-X images acquired on 24 August 2017 and 4 September 2017 in the descending track.

up to 3.5 m on the west-southwest, and of about 2.3 m on the northern slope which were similar to the precedent researches that performed offset tracking technique (Lee et al., 2018; Wang et al., 2018). Hence, the displacement on the ruptured zone of Mt. Mantap appears to descend in the direction of gravity, and

the maximum displacement is locally concentrated on the east-southeast and the west-southwest slope, rather than evenly distributed throughout the whole mountain body. Furthermore, there are many stable areas near the top of the mountain and the middle of slopes that reflect the trend of visual inspection.

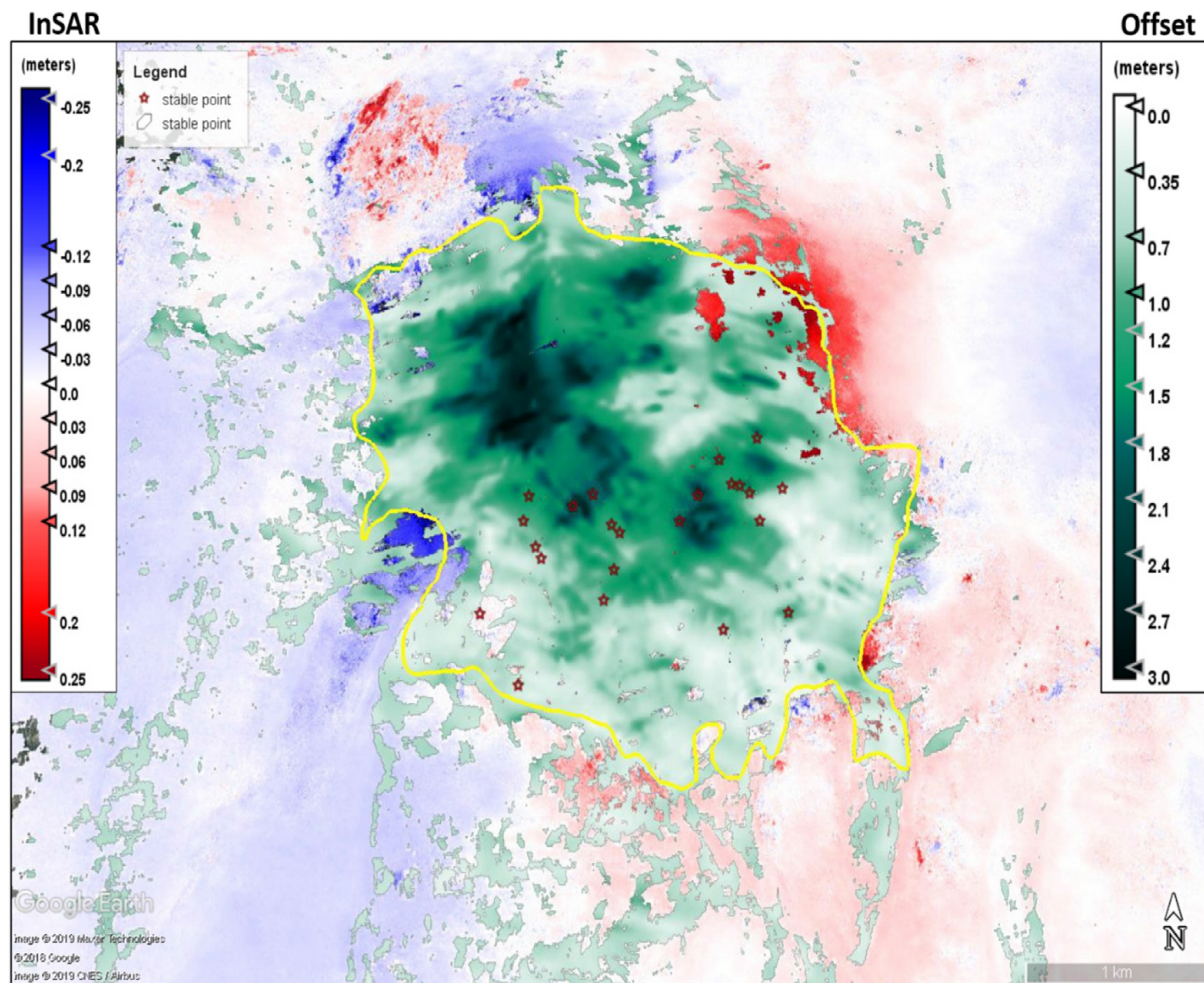


Fig. 8. Overall displacements caused by the 6th nuclear test at Mt. Mantap. The average displacements of offset tracking from ALOS-2 images and the true displacement vector in easting component of InSAR process are combined. The yellow line indicates the boundary between the ruptured zone and the rim part. Red stars indicate the stable points on the mountain slope observed by the visual inspection of TerraSAR-X images.

4.4. Discussion

Overall displacements are shown in Figure 8 that combines the results of the InSAR processing and offset tracking method. The true displacement in easting direction obtained by InSAR process represents the elastic motion of the bedrock outside the rim part where coherence is maintained, while the averaged composite of the offset tracking displacements obtained from ALOS-2 image pairs acquired on 29 August 2017 and 12 September 2017 in the ascending track and on 31 August 2017 and 28 September 2017 in the descending track reflects the land deformation on the ruptured zone in the mountain. The displacement of InSAR process around the rim part can be considered that the mountain bedrock expanded in the radial direction of up to 25 ± 6 cm. On the other hands, offset tracking displacements on the ruptured zone are interpreted as the signal of surficial deformation of up to 2.5 ± 0.6 m on the east-southeast

slope and of up to 3.5 ± 0.6 m on the west-southwest slope toward the direction of gravity. Figure 8 also shows many stable targets along the slopes in the middle of the ruptured zone obtained by visual inspection.

The offset tracking results resemble the previous researches: Wang et al. (2018) reported the surface displacement of up to 3.5 m of divergent horizontal deformation with 0.5 m of subsidence on the top of the mountain were determined by using high-resolution satellite imagery. Lee et al. (2018) also estimated the displacement of up to 3 m on the west slope in azimuth direction by using a multi-kernel pixel tracking method.

Wang et al. (2018) assumed that the bedrock of Mt. Mantap as a symmetric dome, and interpreted the offset tracking results that the displacement is the largest in the centre and weaker in surroundings mostly in the direction of gravity. They modelled that the entire bedrock had undergone the elastic mechanism of the explosion in a radial direction (upward in the centre of the

mountain), and then the direction of the displacement has been changed due to subsequent collapse and compaction of the bedrock.

In this study, the magnitude and the direction of the displacements resemble the former researches. However, we found that displacements were asymmetric throughout the entire bedrock and the maximum displacement occurs on the south-southeast and the west-southwest slope. In addition, many stable and fixed features were observed in the middle of the sliding mountain slopes through visual inspection and offset tracking, which were considered as the bedrock of Mt. Mantap and outcrops. The existence of the stable features strongly indicates that the mechanism on the ruptured zone is likely to be surficial landslides of the unconsolidated topsoil and boulder stones, not an elastic motion such as expansion and compaction. It is suggested that the elastic extensional motion of the bedrock might have been settled back to the origin immediately after the blast or at least during the image taking period used for the offset tracking, or been contaminated by surficial landslides if any. Therefore, the elasticity modelling and the estimation of the location and depth of the explosion sequence might be invalid if deformation caused by landslides is used as an input.

5. CONCLUSION

In this study, we verified surface displacements caused by the 6th nuclear test of North Korea on 3 September 2017 with various approaches of remote sensing. We have attempted to quantitatively interpret surface deformation of Mt. Mantap using high-resolution satellite SAR images. As a consequence of InSAR process, E-W displacements of up to 25 ± 6 cm were observed around the rim part. Similar to the previous results such as Wang (2018) and Lee (2018), the offset tracking in the ruptured zone where the coherence was completely lost shows displacement in the direction of gravity of up to 2.5 ± 0.6 m on the east-southeast slope and of up to 3.5 ± 0.6 m on the west-southwest slope. However, the displacements were locally concentrated and unevenly distributed. Visual inspection on the ruptured zone shows many stable features in the middle of the moving slopes, which is considered as stable bedrocks that do not move within the SAR image accuracy. The existence of stable bedrocks strongly suggests that the observed displacements in the mountain flank are caused by landslides, not the elastic deformation such as expansion, collapse, and compaction of the bedrock as suggested by Wang et al. (2018). Any attempt of elastic modelling of depth and magnitude estimation of the detonation should be limited to the mountain top area only, and would be invalid elsewhere as the observed displacements in the mountain flank might not be the elastic motion of the bedrock but landslides. It might be possible to apply elastic modelling

with the InSAR result outside the rim of the mountain, but the accuracy would be limited because of the limited area. More detailed analysis of the observed displacements and the collection of field data such as the morphology of the bedrock and the topsoil would be beneficial to interpret the event.

ACKNOWLEDGMENTS

This research was supported by the Basic Research Project of Korea Institute of Geoscience and Mineral Resources (KIGAM), funded by the Ministry of Science and ICT of Korea, and the National Research Foundation of Korea (NRF-2019R1F1A1041389, No. 2019R1A6A1A03033167).

REFERENCES

- Bamler, R. and Hartl, P., 1998, Topical review – synthetic aperture radar interferometry. *Inverse Problems*, 14, R1–R54. DOI: 10.1088/0266-5611/14/4/001
- Berardino, P., Fornaro, G., Lanari, R., and Sansosti, E., 2002, A new algorithm for surface deformation monitoring based on small baseline differential SAR interferograms. *IEEE Transactions on Geoscience and Remote Sensing*, 40, 2375–2383. DOI: 10.1109/TGRS.2002.803792
- Chae, S.H., Lee, W.J., Jung, H.S., and Zhang, L., 2017, Ionospheric correction of L-band SAR offset measurements for the precise observation of glacier velocity variations on Novaya Zemlya. *IEEE Journal of Selected Topics in Applied Earth Observations and Remote Sensing*, 10, 3591–3602. DOI: 10.1109/JSTARS.2017.2690799
- Che, I.Y., Park, J., Kim, I., Kim, T.S., and Lee, H.I., 2014, Infrasound signals from the underground nuclear explosions of North Korea. *Geophysical Journal International*, 198, 495–503. <https://doi.org/10.1093/gji/ggu150>
- Chen, C.W. and Zebker, H.A., 2002, Phase unwrapping for large SAR interferograms: statistical segmentation and generalized network models. *IEEE Transactions on Geoscience and Remote Sensing*, 40, 1709–1719. DOI: 10.1109/TGRS.2002.802453
- Curlander, J.C. and McDonough, R.N., 1991, *Synthetic Aperture Radar: Systems and Signal Processing*. John Wiley & Sons, New York, 672 p.
- Ferretti, A., Monti-Guarnieri, A., Prati, C., and Rocca, F., 2007, *InSAR Principles: Guidelines for SAR Interferometry Processing and Interpretation*. ESA Publications, Noordwijk, 252 p.
- Fialko, Y., Sandwell, D., Simons, M., and Rosen, P., 2005, Three-dimensional deformation caused by the Bam, Iran, earthquake and the origin of shallow slip deficit. *Nature*, 435, 295–299. <https://doi.org/10.1038/nature03425>
- Fialko, Y., Simons, M., and Agnew, D., 2001, The complete (3-D) surface displacement field in the epicentral area of the 1999 Mw 7.1 Hector Mine earthquake, California, from space geodetic observations. *Geophysical Research Letters*, 28, 3063–3066. <https://doi.org/10.1029/2001GL013174>
- Glasstone, S. and Dolan, P.J., 1977, *The Effects of Nuclear Weapons* (3rd edition). United States Department of Defence and Department of Energy, Washington, D. C., 653 p.
- Jarvis, A., Reuter, H.I., Nelson, A., and Guevara, E., 2008, Hole-filled

- SRTM for the globe, version 4, CGLAR-CSI SRTM 90m Database. <http://srtm.csi.cgiar.org> [Accessed on 25 September 2020].
- JAXA (Japan Aerospace Exploration Agency), 2014, ALOS-2 Project/PALSAR-2. <http://www.eorc.jaxa.jp/ALOS-2/en/about/palsar2.htm> [Accessed on 25 September 2020].
- Keefer, D.K., 1984, Landslides caused by earthquakes. *Geological Society of America Bulletin*, 95, 406–421.
- Lee, H., 2006, Investigation of SAR systems, technologies and application fields by a statistical analysis of SAR-related journal papers. *Korean Journal of Remote Sensing*, 22, 153–174. (in Korean with English abstract)
- Lee, Y.J., Sun, J.S., Jung, H.S., Park, S.C., Lee, D.K., and Oh, K.Y., 2018, Detection of surface changes by the 6th North Korea nuclear test using high-resolution satellite imagery. *Korean Journal of Remote Sensing*, 34, 1479–1488. (in Korean with English abstract) <https://doi.org/10.7780/kjrs.2018.34.6.4.2>
- Lu, J. and Veci, L., 2016, Sentinel-1 Toolbox: Offset Tracking Tutorial. Array System Computing Inc. and ESA, Toronto, 17 p.
- Ng, A.H.M., Ge, L., Zhang, K., Chang, H.C., Li, X., Rizos, C., and Omura, M., 2011, Deformation mapping in three dimensions for underground mining using InSAR-southern highland coal field in New South Wales, Australia. *International Journal of Remote Sensing*, 32, 7227–7256. <https://doi.org/10.1080/01431161.2010.519741>
- Nitti, D.O., Hanssen, R.F., Refice, A., Bovenga, F., and Nutricato, R., 2011, Impact of DEM-assisted coregistration on high-resolution SAR Interferometry. *IEEE Transactions on Geoscience and Remote Sensing*, 49, 1127–1143. DOI: 10.1109/TGRS.2010.2074204
- NORSAR (Norwegian Seismic Array), 2017, Summing up the nuclear test in North Korea on 3 September 2017. <https://www.norsar.no/i-fokus/summing-up-the-nuclear-test-in-north-korea-on-3-september-2017> [Accessed on 5 October 2020].
- Park, J.H., Park, Y.K., Kim, T.S., Kim, G., Cho, C., and Kim, I., 2017, The analysis on the characteristics of North Korea 6th nuclear test, collapse and induced earthquakes. American Geophysical Union Fall Meeting, New Orleans, Dec. 11–15, #S41G-05.
- Pavian, F.V. and Coblenz, D., 2017, Surface disturbances at the Punggye-ri nuclear test site: another indicator of nuclear testing? U.S. Department of Energy Office of Scientific and Technical Information, Washington, D.C., 12 p. <https://doi.org/10.2172/1342851>
- Sánchez-Gómez, P. and Navarro, E., 2017, Glacier surface velocity retrieved using D-InSAR and offset tracking techniques applied to ascending and descending passes of Sentinel-1 data for southern Ellesmere ice caps, Canadian Arctic. *Remote Sensing*, 9, 442. <https://doi.org/10.3390/rs9050442>
- Shi, X., Zhang, L., Balz, T., and Liao, M., 2015, Landslide deformation monitoring using point-like target offset tracking with multi-mode high-resolution TerraSAR-X data. *ISPRS Journal of Photogrammetry and Remote Sensing*, 105, 128–140. <https://doi.org/10.1016/j.isprsjprs.2015.03.017>
- Song, S.G. and Lee, H., 2018, Static slip model of the 2017 M_w 5.4 Pohang, South Korea, earthquake constrained by the InSAR data. *Seismological Research Letters*, 90, 140–148. <https://doi.org/10.1785/0220180156>
- Stevens, J.L. and O'Brien, M., 2018, 3D nonlinear calculation of the 2017 North Korean nuclear test. *Seismological Research Letters*, 89, 2068–2077. <https://doi.org/10.1785/0220180099>
- Teller, E., Talley, W., Higgins, G.H., and Johnson, G.W., 1968, *The Constructive Uses of Nuclear Explosives* (1st edition). McGraw-Hill, New York, 320 p.
- Tian, D., Yao, J., and Wen, L., 2018, Collapse and earthquake swarm after North Korea's 3 September 2017 nuclear test. *Geophysical Research Letters*, 45, 3976–3983. <https://doi.org/10.1029/2018GL077649>
- USGS (United States Geological Survey), 2017, M 6.3 Nuclear Explosion – 21Km ENE of Sungjibaegam, North Korea. <https://earthquake.usgs.gov/earthquakes/eventpage/us2000aert/executive> [Accessed on 2 October 2020].
- Veci, L., 2016, Sentinel-1 Toolbox: Interferometry Tutorial. Array Systems Computing Inc. and ESA, Toronto, 41 p.
- Vincent, P., Buckley, S.M., Yang, D., and Carle, S.F., 2011, Anomalous transient uplift observed at the Lop Nor, China nuclear test site using satellite radar interferometry time-series analysis. *Geophysical Research Letters*, 38, L23306. <https://doi.org/10.1029/2011GL049302>
- Vincent, P., Larsen, S., Galloway, D.L., Laczniak, R.J., Walter, W.R., Foxall, W., and Zucca, J.J., 2003, New signatures of underground nuclear tests revealed by satellite radar interferometry. *Geophysical Research Letters*, 30, 1–5. <https://doi.org/10.1029/2003GL018179>
- Wang, T., Shi, Q., Nikkhoo, M., Wei, S., Barbot, S., Dreger, D., Bürgmann, R., Motagh, M., and Chen, Q.F., 2018, The rise, collapse, and compaction of Mt. Mantap from the 3 September 2017 North Korean nuclear test. *Science*, 361, 166–170. <https://doi.org/10.1126/science.aar7230>
- Wei, M., 2017, Location and source characteristics of the 2016 January 6 North Korean nuclear test constrained by InSAR. *Geophysical Journal International*, 209, 762–769. <https://doi.org/10.1093/gji/ggx053>
- Wright, T.J., Parsons, B.E., and Lu, Z., 2004, Toward mapping surface deformation in three dimensions using InSAR. *Geophysical Research Letters*, 31, L01607. <https://doi.org/10.1029/2003GL018827>
- Yan, S., Guo, H., Guang, L., and Ruan, Z., 2013, Mountain glacier displacement estimation using a DEM-assisted offset tracking method with ALOS/PALSAR data. *Remote Sensing Letters*, 4, 494–503. <https://doi.org/10.1080/2150704X.2012.754561>
- Yoon, G.W., Koh, J.W., and Lee, Y.W., 2010, Investigation of applications technology for high resolution SAR images. *Journal of the Korea Institute of Military Science and Technology*, 13, 105–113. (in Korean with English abstract)
- Yoon, J. and Lee, H., 2019, Surface change of the 6th nuclear test of North Korea on 3 September 2017 detected by using SAR images. *International Geoscience and Remote Sensing Symposium 2019 (Abstract)*, Yokohama, Jul. 28–Aug. 2, p. 9699–9701. DOI: 10.1109/IGARSS.2019.8900378
- Zhang, M. and Wen, L., 2013, High-precision location and yield of North Korea's 2013 nuclear test. *Geophysical Research Letters*, 40, 2941–2946. <https://doi.org/10.1002/grl.50607>
- Zhou, X., Chang, N.B., and Li, S., 2009, Applications of SAR interferometry in earth and environmental science research. *Sensors*, 9, 1876–1912. <https://doi.org/10.3390/s90301876>